Persistent Ocean Anomalies as a Response to Northern Hemisphere Heating Induced by Biomass Burning Variability

RYOHEI YAMAGUCHI,[a] JI-EUN KIM,[b,c] KEITH B. RODGERS,[b,c] KARL STEIN,[b,c] AXEL TIMMERMANN,[b,c] SUN-SEON LEE,[b,c] LEI HUANG,[d] MALTE F. STUECKER,[e] JOHN T. FASULLO,[f] GOKHAN DANABASOGLU,[f] CLARA DESER,[f] JEAN-FRANCOIS LAMARQUE,[f] NAN A. ROSENBLOOM,[f] AND JIM EDWARDS[f]

[a] *Research Institute for Global Change, Japan Agency for Marine-Earth Science and Technology, Yokosuka, Japan*
[b] *Center for Climate Physics, Institute for Basic Science, Busan, South Korea*
[c] *Pusan National University, Busan, South Korea*
[d] *College of Resource Environment and Tourism, Capital Normal University, China*
[e] *Department of Oceanography and International Pacific Research Center, School of Ocean and Earth Science and Technology, University of Hawai'i at Mānoa, Honolulu, Hawaii*
[f] *Climate and Global Dynamics Laboratory, National Center for Atmospheric Research, Boulder, Colorado*

(Manuscript received 16 February 2023, in final form 3 July 2023, accepted 30 August 2023)

ABSTRACT: Biomass burning aerosol (BBA) emissions in the Coupled Model Intercomparison Project phase 6 (CMIP6) historical forcing fields have enhanced temporal variability during the years 1997–2014 compared to earlier periods. Recent studies document that the corresponding inhomogeneous shortwave forcing over this period can cause changes in clouds, permafrost, and soil moisture, which contribute to a net terrestrial Northern Hemisphere warming relative to earlier periods. Here, we investigate the ocean response to the hemispherically asymmetric warming, using a 100-member ensemble of the Community Earth System Model version 2 Large Ensemble forced by two different BBA emissions (CMIP6 default and temporally smoothed over 1990–2020). Differences between the two subensemble means show that ocean temperature anomalies occur during periods of high BBA variability and subsequently persist over multiple decades. In the North Atlantic, surface warming is efficiently compensated for by decreased northward oceanic heat transport due to a slowdown of the Atlantic meridional overturning circulation. In the North Pacific, surface warming is compensated for by an anomalous cross-equatorial cell (CEC) that reduces northward oceanic heat transport. The heat that converges in the South Pacific through the anomalous CEC is shunted into the subsurface and contributes to formation of long-lasting ocean temperature anomalies. The anomalous CEC is maintained through latitude-dependent contributions from narrow western boundary currents and basinwide near-surface Ekman transport. These results indicate that interannual variability in forcing fields may significantly change the background climate state over long time scales, presenting a potential uncertainty in CMIP6-class climate projections forced without interannual variability.

KEYWORDS: Ocean dynamics; Ekman pumping; Thermohaline circulation; Aerosols; Anthropogenic effects/forcing; Heat budgets/fluxes

1. Introduction

Aerosol forcings in the latest phase of the Coupled Model Intercomparison Project (CMIP6; Eyring et al. 2016) protocol include contributions from biomass burning aerosol (BBA) emissions and a variety of other anthropogenic aerosol emissions (including fluxes from industrial activities and land/marine transport) in addition to natural emissions (dimethyl sulfide, biogenic aerosols, etc.). Although the total amount of global BBA emissions over the recent historical period is smaller than other anthropogenic emissions, the year-to-year variability of BBA emissions is relatively large (Fig. 1a). Fires, the main source of BBA emissions, have a spatially heterogenous distribution and temporal variations caused by changes in vegetation productivity, human activity, climate, and interactions between them (Archibald et al. 2013; van der Werf et al. 2017). BBA emissions forcing data in CMIP6 (BB4CMIP6; van Marle et al. 2017), spanning 1750 to the present, are based on a multimodel mean flux estimated from the Fire Model Intercomparison Project (FireMIP; Rabin et al. 2017). Satellite-derived observational products [Global Fire Emissions Database version 4s (GFED4), for 1997 onward], charcoal datasets (in temperate and boreal regions), and visibility records (in the arc of deforestation and equatorial Asia from the 1960s to 1997) are also incorporated in the BB4CMIP6 (van Marle et al. 2017). The use of observational data that are only available over recent decades, in particular, over the satellite era (from 1997 onward), provides more globally realistic emissions data but also results in inhomogeneities in the amplitude of temporal variability that are a consequence of splicing together disparate types of historical reconstructions (van Marle et al. 2017). Variability in BBA emissions is greater during the recent historical period when large-scale observations are more

Denotes content that is immediately available upon publication as open access.

Supplemental information related to this paper is available at the Journals Online website: https://doi.org/10.1175/JCLI-D-23-0090.s1.

Corresponding author: Ryohei Yamaguchi, ryamaguchi@jamstec.go.jp

DOI: 10.1175/JCLI-D-23-0090.1

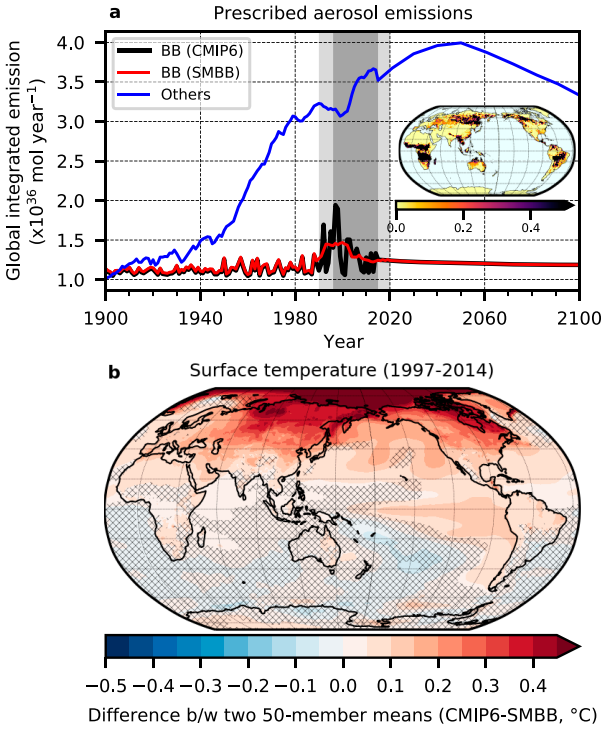

FIG. 1. (a) Globally integrated CMIP6 aerosol emissions from biomass burning (BB; black) and other anthropogenic sources (blue). Temporally smoothed BB aerosol emissions over the period of the large temporal variability (1990–2020; light-gray-shaded period) used in this study are superimposed as a red line [BB (SMBB)]. The dark-gray-shaded period is when the satellite (GFED4) observed data were used (1997–2014). The inserted map shows BB (CMIP6) aerosol emission climatology for 1990–2020 (10^{11} mol cm^2 s^{-1}). (b) Surface (radiative) temperature differences between two subensemble means of a 50-member set forced by BB (CMIP6) and another 50-member set forced by BB (SMBB) from the CESM2-LE. Statistically insignificant differences at the 95% confidence level are cross-hatched. See the details of the experimental settings and the statistical tests in section 2.

directly incorporated into the products, although the net amount (long-term mean) of BBA emissions does not vary dramatically over time (Fig. 1a; see also Fig. S1a in the online supplemental material). The spurious change in the amplitude of interannual BBA emissions is a new feature of CMIP6 forcing that was not present in CMIP5, in which decadal mean fluxes were used to construct BBA emissions (Lamarque et al. 2010).

Several recent model studies with the Community Earth System Model version 2 (CESM2) have shown that high-amplitude interannual variability in BBA emissions can affect not only climate variability for model-simulated fields, but also their longer-timescale variability and mean state. This effect is manifested for instance in 2-m air temperature (Fasullo et al. 2022; Kim et al. 2023) and Arctic sea ice (DeRepentigny et al. 2022), as well as the global hydrological cycle (Heyblom et al. 2022). In particular, in the high-latitude Northern Hemisphere (NH), where there are many prescribed sources of BBA emissions in the climate model (Fig. 1a and Fig. S1b), an increase in BBA emissions variability from 1997 onward causes a net thinning of clouds, thereby enhancing incident shortwave radiation, which in turn warms the surface in the NH (Fasullo et al. 2022). The interannual temperature fluctuations generated by the increased satellite-era BBA variability can be further rectified into a long-term terrestrial warming through permafrost melting and soil moisture changes (Fig. 1b and see also Kim et al. 2023). As the NH warming expands widely beyond the localized sources of anomalous BBA emissions, it induces anomalous Arctic sea ice loss in CMIP6 historical simulations that was absent in CMIP5 simulations (DeRepentigny et al. 2022). In turn these processes can further contribute to shifts in the global-scale hydrological cycle (Heyblom et al. 2022).

It is generally known that hemispherically asymmetric radiative forcing (provided through changes in orbital forcing, albedo, aerosol forcing, or other drivers) leads to interhemispheric thermal gradients and the coupled ocean–atmosphere system works to reduce these gradients [see reviews by Chiang and Friedman (2012), Schneider et al. (2014), and Kang (2020)]. In the atmosphere, anomalous interhemispheric thermal gradients lead to compensating cross-equatorial heat transport (CEHT) by Hadley circulation adjustments and corresponding meridional shifts of the intertropical convergence zone (ITCZ) (Broccoli et al. 2006; Kang et al. 2008). As for the ocean, compensating CEHT is supplied by anomalies in meridional overturning circulation (MOC) and/or anomalies in the shallow subtropical cell structures that are partly coupled to perturbations in the atmospheric Hadley cell (Green and Marshall 2017; Schneider 2017; Kang et al. 2018). A number of studies since the early 1980s have improved our understanding of the global response to the hemispherically asymmetric forcings. However, the role of the ocean in determining the global response remains relatively unexplored (Kang 2020), despite the fact that its importance is well recognized (e.g., Deser et al. 2015; Yoshimori et al. 2018; Kang et al. 2021).

The objective of this study is to identify and understand how the anomalous year-to-year BBA CMIP6 forcing translates into anomalous ocean signals that persist beyond interannual time scales. Our study complements the work of Kim et al. (2023), which focuses on the mechanisms that support shorter-time-scale rectified land surface responses (i.e., warming) over the NH. As with the study of Kim et al. (2023), we use output from the Community Earth System Model version 2 Large Ensemble simulations (CESM2-LE; Rodgers et al. 2021). The 100-ensemble-member CESM2-LE comprises two sets of 50-ensemble-member experiments (referred to as subensembles hereafter), integrated from 1850 to 2100 with the CMIP6 historical (1850–2014) and the Shared Socioeconomic Pathway 3–7.0 (SSP3–7.0) (2015–2100) scenarios with different BBA forcings. For the BBA forcing, the first 50 members are forced with the default CMIP6 BBA forcing (BB4CMIP6) and the remaining 50 members use temporally smoothed BB4CMIP6 for the period of high-amplitude interannual variability (1990–2020) (Fig. 1a and Fig. S1a; details in section 2). By taking ensemble averages across each 50-member subensemble and differencing them, one can extract the forced signal due to the difference of BBA forcings from the background noise associated with internal variability. Comparison of the two subensemble averages reveals the presence of ocean anomalies that are induced by the

large BBA emissions variability and their persistence over several decades beyond the period of different BBA forcing. The comparison also shows previously reported NH atmospheric warming and Arctic sea ice melting (see section 3 for details).

After describing the details of the model experimental design and the statistical methods used in this study in section 2, we show comparisons of the two subensemble mean fields and the atmosphere–ocean responses to the decadal NH warming from the perspective of the energy budgets in section 3. In section 4, we provide a mechanistic account of the ocean's role in compensating for the interhemispheric thermal gradient set by the high-amplitude interannual variability of the BBA forcing. The results are summarized along with a discussion of implications in section 5.

2. Data and methods

We use output from the 100-member large ensemble (LE) conducted using CESM2 (Danabasoglu et al. 2020) as part of a collaboration between the Institute for Basic Science (IBS) Center for Climate Physics and the CESM2 initiative at the National Center for Atmospheric Research (NCAR). CESM2 is a CMIP6-generation Earth system model developed at NCAR in collaboration with the broader community. It comprises the Community Atmosphere Model version 6 (CAM6; Bogenschutz et al. 2018), the Community Land Model version 5 (CLM5; Lawrence et al. 2019), the Parallel Ocean Program version 2 (POP2; Smith et al. 2010; Danabasoglu et al. 2012), and the Community Ice Code version 5 (CICE5; Hunke et al. 2015). CAM6 has a resolution of 1.25° in longitude and 0.9° in latitude with 32 vertical levels. CLM5 has the same horizontal grid as CAM6. POP2 and CICE5 share the same horizontal grid, with a uniform spacing of 1.125° in the zonal direction and varying in the meridional direction from 0.65° at high and midlatitudes to 0.25° at the equator; POP2 has 60 vertical levels (20 of these are in the upper 200 m of the water column).

Initial conditions for the 100-member LE are a mixture of "macro–" and "micro–" perturbation initializations (Rodgers et al. 2021). Twenty macro–perturbation initial conditions were selected at 10-yr intervals from starting points at least 1000 years into the CESM2 preindustrial simulation (Danabasoglu et al. 2020). By adding small round-off level perturbations to the atmospheric potential temperature field, 20 micro–perturbation initial conditions were created from each of the additional four macro–perturbation initial conditions (4×20 micro–perturbation initial conditions). The four additional macro–initial states were chosen based on conditions of the Atlantic meridional overturning circulation (AMOC) [see Rodgers et al. (2021) for details] from the preindustrial simulation. All members were integrated from 1850 to 2100 with common forcings of the CMIP6 historical simulations for the period from 1850 to 2014 and the SSP3–7.0 scenario for the later period, except for the BBA forcing. Any climate state differences among members originating from differences in the initial conditions are negligible for the period of interest in this study (from 1990 onward; i.e., 140 years after the initialization). Indeed, the initial condition dependence of the AMOC, which could have a relatively long memory, drops below the detection limit within a few decades (Rodgers et al. 2021, their Fig. S2).

The 100-member LE comprises two subensembles of 50 members each, with each subensemble distinguished by its BBA forcing over 1990–2020. The first 50 members are compliant with CMIP6 forcing protocols, thereby including high-amplitude BBA emissions variability, with this subensemble henceforth referred to as the CMIP6 subensemble. The second group of 50 members uses temporally smoothed CMIP6 BBA forcing over the period 1990–2020 and is henceforth referred to as the SMBB subensemble. The temporal smoothing was performed with an 11-yr moving average applied separately for each month of the monthly averaged time series to preserve the seasonal cycle. We emphasize that as a simple moving average was applied, the net integrated BBA emissions over the period of interest are nearly conserved between the two forcings (Fig. S1). In addition to the difference in BBA forcing, some slight corrections of forcings and code modifications, mainly in CLM5, were applied for the SMBB subensemble [see section 2.4 in Rodgers et al. (2021) for details]. The impact from these additional modifications is rather minor with no apparent effects on the climate mean state. For the purposes of this study, we base our interpretation on the assumption that the differences between the two subensemble means after year 1990 can be attributed mainly to the differences in the temporal variability of BBA forcing over 1990–2020.

To determine if a difference between subensemble means is statistically significant, we use a bootstrap-like method to utilize information on background internal variability which can be estimated from the LE members. Considering that some of the diverse range of variables examined in this study may not necessarily exhibit internal variability according to a normal distribution, we chose a nonparametric method here to ensure consistency of the statistical test across the variables. We first randomly select two groups of 50 members from the 100-member LE and compute the difference between the means of the two groups. Repeating the computation 10 000 times, we calculate the standard deviation of the 10 000 differences, and the sampling distribution of the differences converging to the standard normal distribution as the number of trials increases. For the case where the difference between the CMIP6 subensemble mean and SMBB subensemble mean (referred to as the 50–50 difference) is outside the range of twice the standard deviation of the 10 000 random differences, the 50–50 difference is defined as statistically significant at the 95% confidence level; that is, it is not likely to occur by chance due to the background internal variability.

3. Impacts of high-amplitude interannual variability in BBA emissions

a. *Anomalous heat entering into the Earth system*

Statistically significant CMIP6 versus SMBB differences in several climatological metrics are seen during and beyond the period of different BBA forcing (1990–2020) in Fig. 2. In terms of the global energy budget, a relative excess of heat enters the Earth system in the form of radiative fluxes through

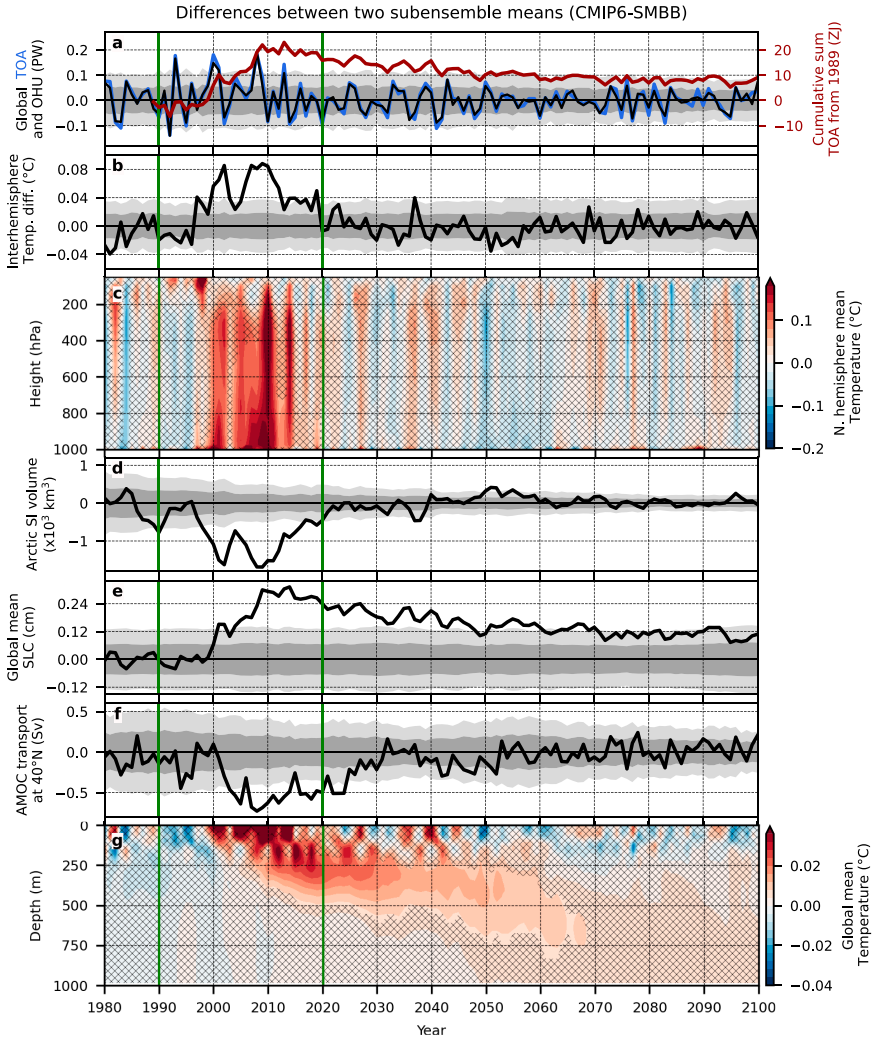

FIG. 2. Differences in subensemble means (CMIP6 minus SMBB) for (a) globally integrated top-of-atmosphere radiation imbalance (TOA; blue line) and ocean heat uptake (OHU; i.e., net ocean surface heat flux; black line), (b) interhemispheric difference in column-mean atmospheric temperature (NH minus SH), (c) NH mean atmospheric temperature profiles, (d) Arctic sea ice (SI) volume, (e) global mean steric sea level change (SLC; estimated from seawater density changes), (f) AMOC maximum transport at 40°N defined from the AMOC mass streamfunction, and (g) global mean ocean temperature profiles. In (a), the cumulative sum of TOA difference from 1989 (red line, right axis) is also shown. The time interval surrounded by two green lines corresponds to the time interval where CMIP6 and SMBB forcings differ. The estimated range of standard deviations (σ) based on the bootstrapping analysis are shown in (a), (b), and (d)–(f) (dark-gray shading for $\pm\sigma$ and light-gray shading for $\pm 2\sigma$). Statistically insignificant differences at the 95% confidence level are cross-hatched in (c) and (g).

the top of the atmosphere (TOA; up to 0.4 W m^{-2} as an annual mean) in the CMIP6 subensemble (blue line in Fig. 2a). The total amount of heat accumulated from the beginning of the period with different forcing reaches up to 20 ZJ (red line in Fig. 2a). The anomalous heat input from the top of the atmosphere enters as an anomalous shortwave radiative flux, mainly within the NH high latitudes (Figs. 3a–c and 4a). The heat that enters the Earth system serves to immediately warm the atmosphere (Fig. 2c) and to melt Arctic sea ice (Fig. 2d). Although the net integrated BBA emissions are nearly identical between CMIP6 and SMBB subensembles, the nonlinearity in the aerosol–cloud interaction induces the net warming in the NH high latitudes (cf. DeRepentigny et al. 2022, their Fig. 4), and the warming is further rectified though the permafrost feedback resulting in the decadal NH warming (cf. Kim et al. 2023).

In contrast to the rapidity with which the heat enters the system, it is radiated back to space rather slowly (red line in Fig. 2a). Whereas the heat largely enters the Earth system in

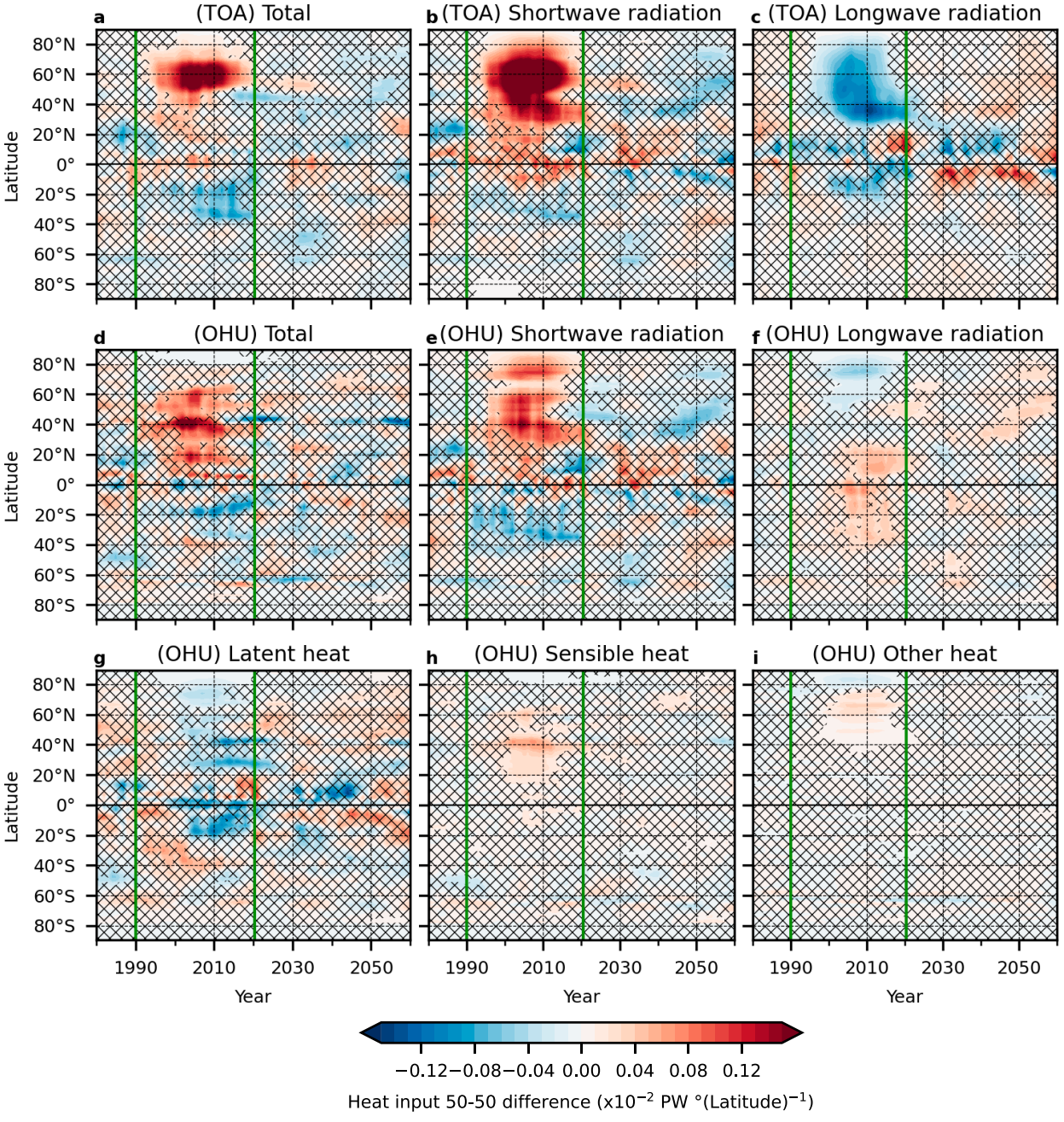

FIG. 3. Differences in subensemble means (CMIP6 minus SMBB) of zonally integrated (a)–(c) top-of-atmosphere radiation imbalance (TOA) and (d)–(i) ocean heat uptake (OHU). TOA consists of (b) shortwave and (c) longwave radiation components and the modeled OHU is decomposed into surface fluxes of (e) shortwave radiation, (f) longwave radiation, (g) latent heat of evaporation, (h) sensible heat, and (i) other heat from sea ice processes and river runoff. An 11-yr running mean is applied for all panels. Positive differences indicate anomalous downward flux (TOA: to the atmosphere; OHU: to the ocean) in the CMIP6 subensemble. The time interval between the two green lines corresponds to when CMIP6 and SMBB BBA forcings are different (1990–2020). Statistically insignificant signals at the 95% confidence level are cross-hatched.

the NH high latitudes, with a maximum spanning from Siberia to North America (Fig. 4a), the regions of anomalous emissions back to space as longwave radiation over 2015–30 occur principally on the eastern flanks of the North Pacific and North Atlantic Oceans (Fig. 4b).

Less than 10% of the total anomalous heat input during 1990–2020 goes to warm the atmosphere and melt sea ice. The vast majority of the anomalous heat (~92%) is rather absorbed by the oceans (black line in Fig. 2a). Preferential ocean heat uptake (OHU; i.e., net air–sea surface heat flux) regions

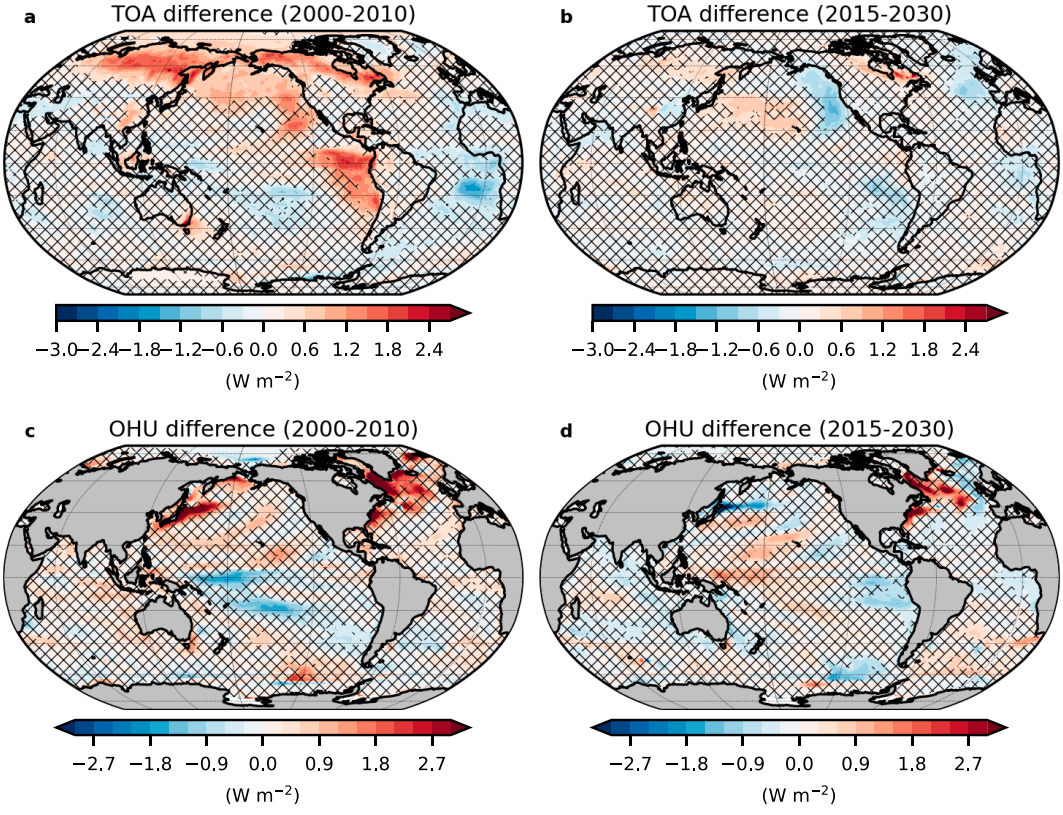

FIG. 4. Differences in top-of-atmosphere radiation imbalance (TOA) and ocean heat uptake (OHU) fluxes between the CMIP6 and SMBB subensemble means. Spatial patterns are shown for the periods of (a),(c) absorbing heat (2000–10) and (b),(d) releasing heat (2015–30), defined based on the global mean TOA flux differences (Fig. 2a). Positive differences indicate anomalous downward fluxes (TOA: to the atmosphere; OHU: to the ocean) in CMIP6 subensemble relative to SMBB subensemble. Statistically insignificant differences at the 95% confidence level are cross-hatched.

include the band represented by the NH trade winds (near 20°N), winter deep convection regions near the western boundary currents (WBCs) in both the North Pacific and Atlantic, and along the Arctic sea ice margin (around 60°N) where sea ice retreats and hence heat exchange is enhanced (Figs. 3d and 4c). Shortwave radiative flux anomalies are the main contributors to anomalous ocean heat uptake (Figs. 3d–i) in the NH high latitudes. The heat taken up by the ocean raises the global mean ocean temperature between the surface and ~700 m depth (Fig. 2g) and expands the ocean, as can be seen with the global mean steric sea level change of 3 mm (Fig. 2e). Previously reported atmospheric and cryosphere anomalies induced by the high-amplitude BBA emissions variability (Fasullo et al. 2022; DeRepentigny et al. 2022; Kim et al. 2023) disappear soon after the end of the period where CMIP6 and SMBB forcings are different (e.g., Figs. 2c,d). In contrast, oceanic thermal anomalies remain in the system for at least several decades, acting as a longer-term memory in the system (e.g., Figs. 2e–g). In the next section, we investigate the mechanisms responsible for generating these long-lasting ocean anomalies by tracking ocean heat anomalies within the ocean interior.

b. *Perturbations to atmospheric and oceanic interhemispheric heat transports*

Increases in the interhemispheric thermal gradient (Fig. 2b) due to hemispherically asymmetric warming anomalies lead to coordinated adjustments of the atmosphere and ocean meridional heat transports (MHTs) that act to reduce the gradient, as has been described in previous studies (e.g., Deser et al. 2015; Green and Marshall 2017; Kang et al. 2021). For our case, where the ocean transports heat northward and the atmosphere transports heat southward across the equator under climatological conditions (Fig. 5a, inset figure), the NH decadal warming anomaly induced by high-amplitude variability in BBA emissions reduces the northward ocean heat transport and increases the southward atmospheric heat transport at the equator (Fig. 5b). As a result, the excess heat added to the NH is compensated or transported to the Southern Hemisphere (SH), thus contributing to decreasing the interhemispheric thermal gradient. Changes in the atmospheric CEHT are linked to changes in the Hadley circulation (Kang et al. 2008; Schneider et al. 2014), which is further manifested by the meridional shift of the ITCZ. Also in the present case,

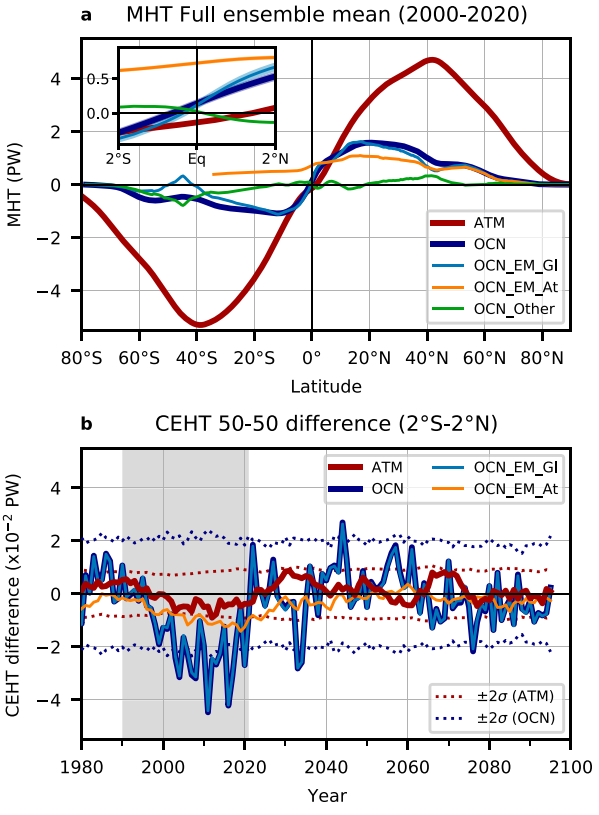

FIG. 5. (a) 100-member ensemble-mean climatology for years 2000–20 (lines) and ensemble spread ($\pm 2\sigma$; shading) of the meridional heat transport (MHT; positive northward) by the atmosphere (ATM) and ocean (OCN). Note that, on most lines, the $\pm 2\sigma$ range is so narrow that it is hidden by the line itself. The ocean MHT is decomposed into the Eulerian-mean circulation component (OCN_EM) and other components (OCN_Other) including the mesoscale eddy (bolus) transport, horizontal diffusion, and parameterized submesoscale transport. The Eulerian component in the Atlantic (OCN_EM_At) is shown separately from the Eulerian component over the global domain (OCN_EM_Gl). The inserted panel in (a) shows an enlarged view of the climatological MHTs near the equator. (b) Differences in cross-equatorial heat transport (CEHT) between CMIP6 and SMBB subensemble means. Note that the OCN and OCN_EM_Gl lines in (b) overlap each other. An 11-yr running mean is applied to the time series. The gray-shaded period corresponds to when CMIP6 and SMBB forcings are different (1990–2020). The estimated two standard deviation ranges ($\pm 2\sigma$) based on bootstrapping are shown as dashed lines.

a northward shift of the ITCZ is identified in the Atlantic and Indian Ocean sectors (Fig. S2b). Changes in the wind-driven component of the ocean CEHT are coupled via the trade winds to changes in the Hadley circulation (Green and Marshall 2017), and for this case the ocean CEHT anomaly occurs in the same direction (southward) as the atmospheric CEHT anomaly (Fig. 5b).

Responses of the oceanic and atmospheric CEHT to hemispherically asymmetric forcings are sensitive to the geographical location and intensity of the forcings (Hawcroft et al. 2018; White et al. 2018; Yu and Pritchard 2019). In the present case, the magnitude of the CEHT anomaly is approximately 5 times larger in the ocean than in the atmosphere, with no phase difference between the two (Fig. 5b). The southward ocean CEHT anomalies are mostly induced by the contribution from the Eulerian-mean (EM) currents, and the other components [mesoscale eddy (bolus) transport, horizontal diffusion, and parameterized submesoscale transport] do not contribute strongly. For the climatological mean behavior of CESM2, CEHT for the Atlantic Ocean is positive (northward heat transport) and CEHT for the Indo-Pacific domain (OC_EM_Gl minus OCN_EM_At in Fig. 5a) is negative (southward heat transport). However, the directions of the anomalous CEHT induced by the high-amplitude BBA emissions variability are southward in both ocean basins. Of the southward ocean CEHT anomaly during years 2000–20, 42% occurs in the Atlantic, and the remaining 58% in the Indo-Pacific (Fig. 5b), with this result standing in contrast to results from a previous study that emphasized the Atlantic contribution under the NH cooling (Yu and Pritchard 2019).

4. Mechanisms for long-lasting ocean anomalies

a. Fate of heat taken up by ocean

The fate of the heat absorbed by the ocean is identified by applying a budget analysis for ocean heat content (OHC) (Fig. 6). For each basin, 50–50 differences in changes in ocean heat content ($d\mathrm{OHC}/dt$; green lines in Fig. 6) should be balanced by 50–50 differences in the sum of the air–sea heat flux at the surface (SHF; orange lines in Fig. 6) and 50–50 differences in the ocean heat transport convergence (OHTC; blue lines in Fig. 6). It should be noted that OHTC is estimated directly from temperature and velocity fields only for those basins where the relevant model output was saved (i.e., only for the North Pacific, North Atlantic, Southern Ocean, and low-latitude Atlantic); otherwise, they are estimated as a residual in the budget analysis. For the full global ocean domain (Fig. 6a, where over the global domain no net OHTC term exists by definition), during the period of high-amplitude variability in BBA emissions (1990–2020), ocean heating of $\sim 6 \times 10^{-2}$ PW occurs, resulting in up to 18 ZJ of anomalous OHC in the CMIP6 subensemble. Subsequently, the global OHC anomaly decreases more slowly than its increase. Although the pattern of ocean heat loss is less coherent than it is for ocean heat uptake, relatively strong heat release can be identified along the Kuroshio/Oyashio Extension region and in the eastern tropical and South Pacific (Fig. 4d). Heat release in these regions is due to decreases in incoming shortwave radiation and anomalous latent heat fluxes, respectively (Figs. 3d–i). While the ocean steadily loses heat after the end of the period, the global OHC anomaly remains statistically significant at the 95% confidence level until the end of the simulation (i.e., year 2100) in association with accumulation of heat below 300 m depth (Fig. 6a).

The North Pacific (Fig. 6d) and North Atlantic (Fig. 6e), where anomalous surface heating due to anomalous BBA forcing is the largest, show seemingly similar basinwide responses. Surface heating in the North Pacific and North Atlantic reaches

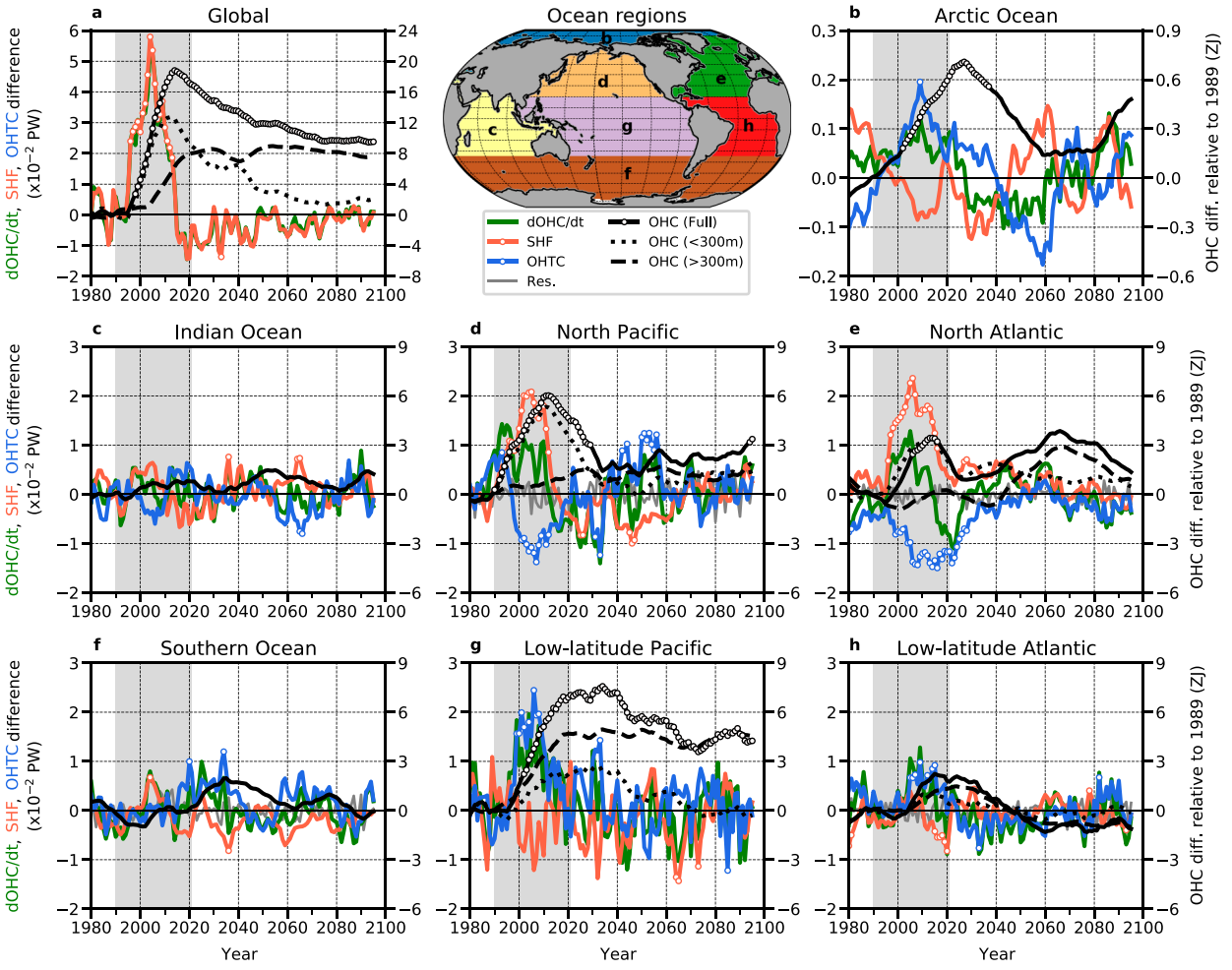

FIG. 6. Budgets for the ocean heat content differences between the CMIP6 and SMBB subensemble means. For (a) the global ocean and (b)–(h) each ocean basin (a spatial map of the different ocean regions is inserted as the upper central panel), 50–50 differences in changes in the full-depth ocean heat content (dOHC/dt), sea surface heat flux (SHF), and ocean heat transport convergence (OHTC) are shown as green, orange, and blue lines with the left y axis, respectively. The residual (Res.) is also shown as a gray line with the left y axis if available. Black solid lines are 50–50 differences in the full-depth OHC (with the right y axis). In the (a) global ocean, (d),(g) Pacific, and (e),(h) Atlantic plots, 50–50 differences in OHCs above 300 m and below 300 m are also shown as dotted and dashed lines with the right y axis, respectively. The Southern Ocean is defined as oceans south of 34°S, and the Pacific and Atlantic are separated into their respective northern and low-latitude parts at 20°N. An 11-yr running mean is applied to all time series. The white dots on the black, blue, and orange lines indicate statistically significant differences at the 95% confidence level based on the bootstrapping method. The gray-shaded period corresponds to the time interval where CMIP6 and SMBB forcing are different (1990–2020).

up to 2×10^{-2} PW during the time of high-amplitude BBA emissions variability, resulting in a corresponding local increase in OHC (until approximately year 2016). In both regions, the negative OHTC anomalies (divergence of ocean heat transport) following the anomalous positive SHF perturbations dominate dOHC/dt. The OHC anomalies themselves return to a statistically insignificant level by the year 2020 for the North Atlantic and by the year 2030 for the North Pacific, although the negative SHF anomalies also partially contribute to the OHC decrease in the North Pacific. Contemporaneously with the negative OHTC anomalies in the North Atlantic (until year 2040), the OHC in the Arctic Ocean significantly increases due to the positive OHTC anomaly (Fig. 6b). On the other hand, positive OHTC anomalies in the low-latitude Atlantic (until year 2020) are subsequently offset by the negative SHF anomalies, and therefore OHC anomalies do not increase to a statistically significant level (Fig. 6h). Positive OHTC anomalies in the low-latitude Pacific, which occur at the same time as negative OHTC anomalies in the North Pacific (in approximately years 2000–10), cause positive OHC anomalies that are the only statistically significant OHC anomalies among ocean regions at the end of the simulation (Fig. 6g). The long-lasting low-latitude Pacific OHC anomalies are largely confined to the subsurface (deeper than 300 m) and account for the largest fraction (50%) of the remaining global OHC anomalies at the end of the simulations.

b. *Ocean basin response for compensating and/or sequestering the heat*

Although for both the North Pacific and the North Atlantic the anomalous heating associated with higher-amplitude variability BBA emissions is compensated by the ensuing OHTC anomalies, the meridional extent of the ocean MHT anomalies is notably different between the two ocean basins. During the latter half of the high-amplitude BBA emissions period (2000–20) when the OHTC anomalies are large, the global ocean MHT anomalies extend broadly from 60°N to the south of 30°S with the dominant contribution from the Eulerian-mean component to its southward anomalies (Fig. 7a). The MHT anomalies for the North Atlantic Ocean are responsible for a portion of the global ocean MHT anomalies broadly from 60°N to at least 30°S. On the other hand, the negative MHT anomalies in the Indo-Pacific basin, mainly caused by the Eulerian-mean component (the difference between OCN_EM_Gl and OCN_EM_At in Fig. 7a), are confined within 30°S–30°N.

The dominant Eulerian-mean components in the MHT anomalies in each basin correspond well to changes in the MOC over each basin. The Atlantic MHT anomalies, which are broadly negative across the basin, share their spatial characteristics with the weakening of the AMOC (Fig. 7b). On the other hand, in the Pacific the shallow subtropical cells (STCs; McCreary and Lu 1994) at low latitudes (30°S–30°N) weaken in the NH and strengthen in the SH during the latter half of the period of the high-amplitude BBA emissions (Fig. 7c). The combined effect of the STC anomalies in both hemispheres result in an anomalous cross-equatorial cell (CEC; Miyama et al. 2003) that comprises ascending branches in the NH subtropics connecting to southward surface currents across the equator and descending branches in the SH subtropics feeding northward subsurface currents back into the NH. Southward surface current anomalies at the equator, corresponding to the upper branch of the CEC, are consistent with the southward MHT anomalies in the Pacific Ocean. These basin contrasts of the MOC responses have also been identified in previous studies that evaluated the response of climate models to hemispherically asymmetric cooling (e.g., Green and Marshall 2017; Yu and Pritchard 2019; Kang et al. 2021).

1) ATLANTIC

From a temporal perspective, the North Atlantic OHTC anomalies in Fig. 6e are also consistent with the AMOC anomalies. In the subensemble members forced with high-amplitude variability in BBA emissions (CMIP6 subensemble), the AMOC transport, assessed at the latitude where it is maximum (40°N), is ~0.7 Sv (1 Sv $\equiv 10^6$ m^3 s^{-1}) smaller than that in the SMBB subensemble not only during the period where CMIP6 and SMBB forcing differ but also thereafter (Fig. 2f). The AMOC anomalies are also largest at 40°N and extend meridionally across the Atlantic basin from the 2000s to the 2030s, and eventually disappear completely by the 2040s (Fig. S3). In terms of the heat budget, the AMOC anomalies compensate for the anomalous surface heat input into the North Atlantic by reducing mean northward ocean heat transport (i.e., a southward ocean MHT anomaly is induced).

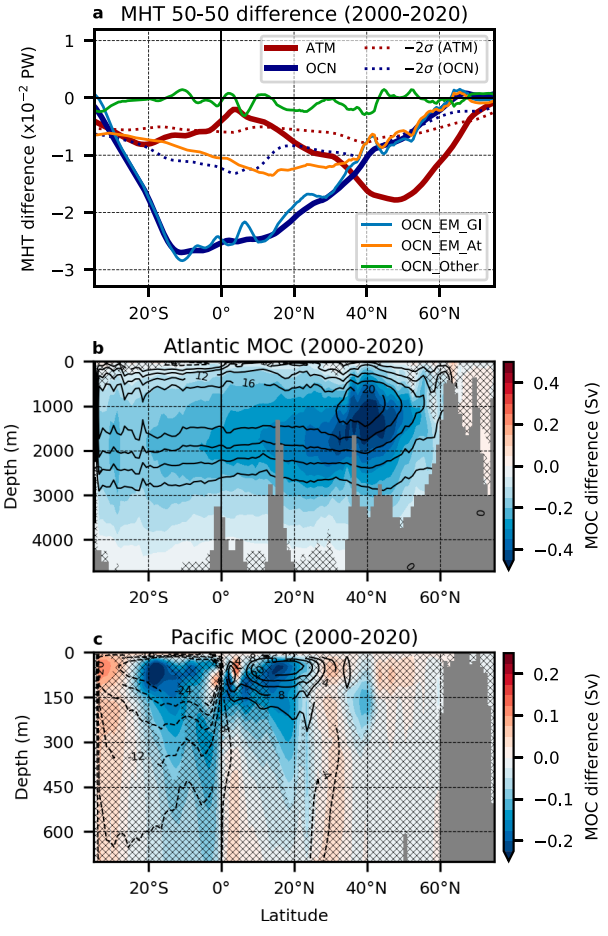

FIG. 7. Differences in subensemble means (CMIP6 minus SMBB) for (a) meridional heat transport (MHT) and (b) Atlantic and (c) Pacific meridional overturning circulation (MOC; positive clockwise). Line colors in (a) are as in Fig. 5. The 100-member ensemble-mean climatology of MOC streamlines (2000–20, Sv) is superimposed as contours in (b) and (c). Statistically insignificant differences at the 95% confidence level are cross-hatched in (b) and (c).

The weakening of the AMOC during and after the period of the high-amplitude variability in BBA emissions is likely due to the suppression of winter convection (Fig. S2d) associated with anomalous surface buoyancy gain. On decadal time scales, sea surface buoyancy (freshwater and heat) forcing in the North Atlantic deep convection sites is one of the key factors driving AMOC variability in model simulations (Timmermann et al. 1998; Biastoch et al. 2008; Yeager and Danabasoglu 2014; Pillar et al. 2016). High-amplitude BBA emissions variability leads to reduced sea ice formation (Fig. 2d and Fig. S2f) and thereby to a net buoyancy gain due to fresher surface waters to the north of 75°N in the Arctic, while at the same time over 65°–75°N there is a net buoyancy loss with the decrease in surface freshwater due to the reduced supply of ice (Figs. S4a,b). However, in the regions where deep convection occurs in this

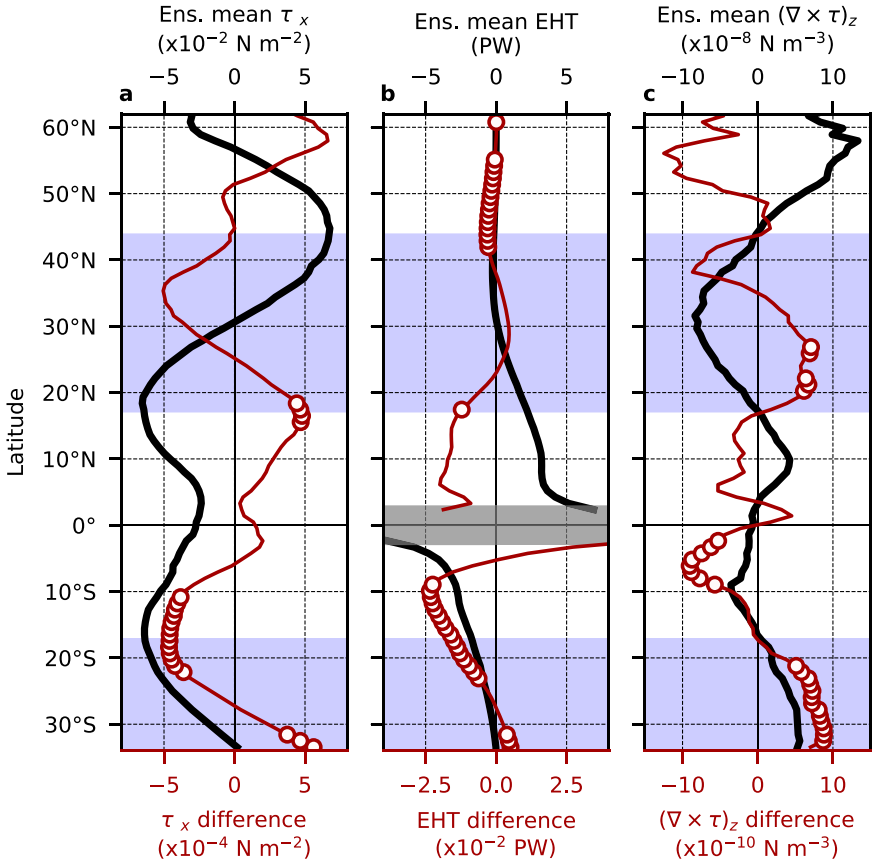

FIG. 8. Pacific 100-member ensemble-mean climatology (black lines with upper x axis) and subensemble-mean difference (CMIP6 minus SMBB; red lines with bottom x axis) in (a) zonal-mean zonal wind stress (τ_x; positive eastward), (b) zonally integrated meridional Ekman heat transport (EHT; positive northward), and (c) zonal-mean surface wind stress curl [$(\nabla \times \boldsymbol{\tau})_z$] over years 2000–20. Blue-shaded latitudes represent the subtropics in each hemisphere defined from the climatology of zonal-mean surface wind stress curl. The white dots on the differences (red lines) indicate statistically significant differences at the 95% confidence level based on the bootstrapping method.

model (the Labrador Sea and the Irminger Sea; Fig. S2c), the buoyancy gain due to surface heating overcomes the freshwater component of the buoyancy flux anomalies (Fig. S4). As a result, surface buoyancy forcing is positive (ocean buoyancy gain), implying enhanced upper ocean stratification and suppressed winter convection that can lead to a slowdown of the AMOC.

2) PACIFIC

The Pacific STC anomalies (i.e., an anomalous CEC structures) correspond well with zonal wind anomalies, as documented in previous studies with idealized atmosphere–ocean coupled models (Green and Marshall 2017). During the period when CMIP6 and SMBB forcings differ, the trade wind 50–50 differences are largest at the latitudes of their climatological maxima (approximately 18°N and 18°S), with a weakening in the NH and strengthening in the SH (Fig. 8a). As a result, meridional Ekman heat transport calculated from the zonal wind stress anomalies and ocean temperature (Sato et al. 2002) shows southward anomalies in both the NH and SH, except for latitudes close to and on the equator (Fig. 8b). This is consistent with the Pacific Ocean MHT anomalies and zonal-mean circulation anomalies seen in Figs. 7a and 7c, respectively. This seems to provide favorable conditions for the anomalous southward Pacific Ocean CEHT to compensate for the NH decadal warming induced by the BBA emissions variability differences, although such a relationship is not apparent in the Atlantic (Fig. S5). Indeed, previous studies (Green and Marshall 2017; Kang et al. 2018) have proposed that mechanistic coupling with changes in the Pacific Ocean trade winds (i.e., Hadley circulation) could form an ocean CEC through Ekman dynamics and create ocean CEHT anomalies in the same direction as the atmosphere.

However, the actual current fields that constitute the Pacific STCs are complicated, and the STCs and the associated MHTs are not fully explained by the near-surface Ekman heat transports alone that are directly driven by local trade winds. Factors

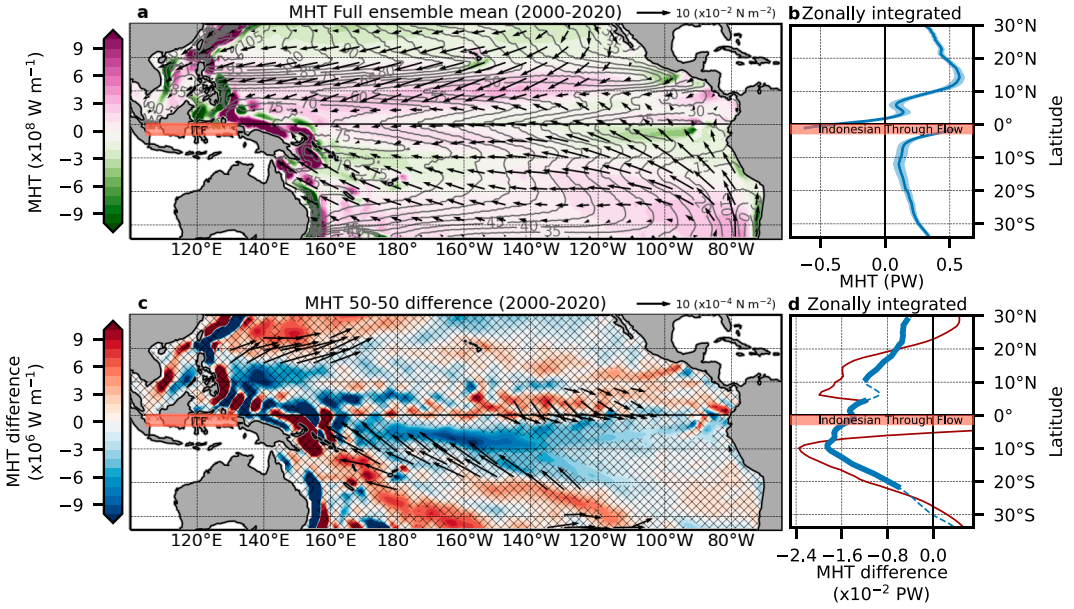

FIG. 9. (a) 100-member ensemble-mean climatology (2000–20) and (c) subensemble-mean difference (CMIP6 minus SMBB) in ocean full-depth meridional heat transport (MHT; positive northward) and surface wind stress. Zonally integrated MHT ensemble-mean climatology [blue line with shading (the range of the two ensemble standard deviations)] and its 50–50 difference are shown in (b) and (d), respectively. The 100-ensemble-mean climatology of sea surface height (SSH; in cm) is shown as contours in (a). The 50–50 difference of the meridional Ekman heat transport (EHT; same as Fig. 8b) is also shown as the red line in (d). In (c), statistically insignificant MHT differences at the 95% confidence level are cross-hatched and only wind stress differences for which the zonal components are statistically significant at the 95% confidence level are shown. Statistically significant zonally integrated MHT differences are shown as thick solid lines in (d).

that play a dominant role in the net northward basinwide (zonally integrated) Pacific MHT reflect a complex interplay between narrow WBCs and broad near-surface currents away from the western boundary (non-WBCs), with the relative contributions being latitude-dependent (Figs. 9a,b). Over the latitudes of the North Pacific subtropical gyre (north of 20°N), northward transport by the WBC (Kuroshio) contributes dominantly to the net northward MHT. In the lower latitudes of the North Pacific comprising the tropical circulation system, including the southward-flowing equatorial WBC (Mindanao Current) but excluding the equatorial waveguide region (3°N–3°S), northward Ekman heat transport in the non-WBC region due to prevailing trade winds forms the net northward MHT. In the SH, the northward MHT by the northward WBCs of the tropical circulation system [the New Guinea Coastal Undercurrent (NGCU) and North Queensland Current/Hiri Current (NQC/HC); cf. Cravatte et al. 2011] is dominant equatorward of 18°S, while the non-WBC northward heat transport is dominant in the subtropical gyre (at least, north of 34°S as shown in Fig. 9a), resulting in the net northward basin-integrated MHT over all latitudes for the SH.

As was the case with the climatological currents, the southward MHT anomalies due to the BBA-induced anomalous Pacific CEC reveal latitude dependence (Figs. 9c,d). In the North Pacific subtropical gyre (north of 20°N), anomalous ocean meridional heat flux (MHF) by the WBCs is the principal contributor to the Pacific basin's net southward MHT anomalies (Fig. 10a). The northward MHT by the North Pacific subtropical WBC (the Kuroshio) is weakened, such that the zonally integrated MHT anomalies are southward over the respective latitudes. On the other hand, over the equatorward portion of the South Pacific subtropical gyre (18°–30°S), anomalous southward MHF due to a strengthened South Pacific subtropical WBC (the Eastern Australian Current) contributes to the basinwide southward MHT anomalies over the respective latitudes (Fig. 10e). These WBC transport changes are driven by anomalies in the surface wind stress curl and its zonal integral (Fig. 8c). In other words, the North Pacific subtropical gyre weakens and the South Pacific subtropical gyre strengthens.

In contrast to the subtropics, over the latitudes associated with the tropical circulation system, MHT anomalies promoted through the Ekman heat transport in non-WBC regions play an important role in generating the net southward Pacific basin MHT anomalies (Fig. 9d). In the North Pacific component of the tropical Pacific circulation (2°–18°N), reduced northward Ekman heat transport due to weakened trade winds to the east of 130°E contributes to the net southward zonally integrated MHT anomaly (Fig. 10b). For the South Pacific component of the tropical Pacific circulation (2°–16°S), the net southward zonally integrated MHT anomalies are caused mainly by enhanced southward Ekman heat transport due to trade wind strengthening, a characteristic that is widely distributed over the ocean basin at 10°S (Fig. 10d).

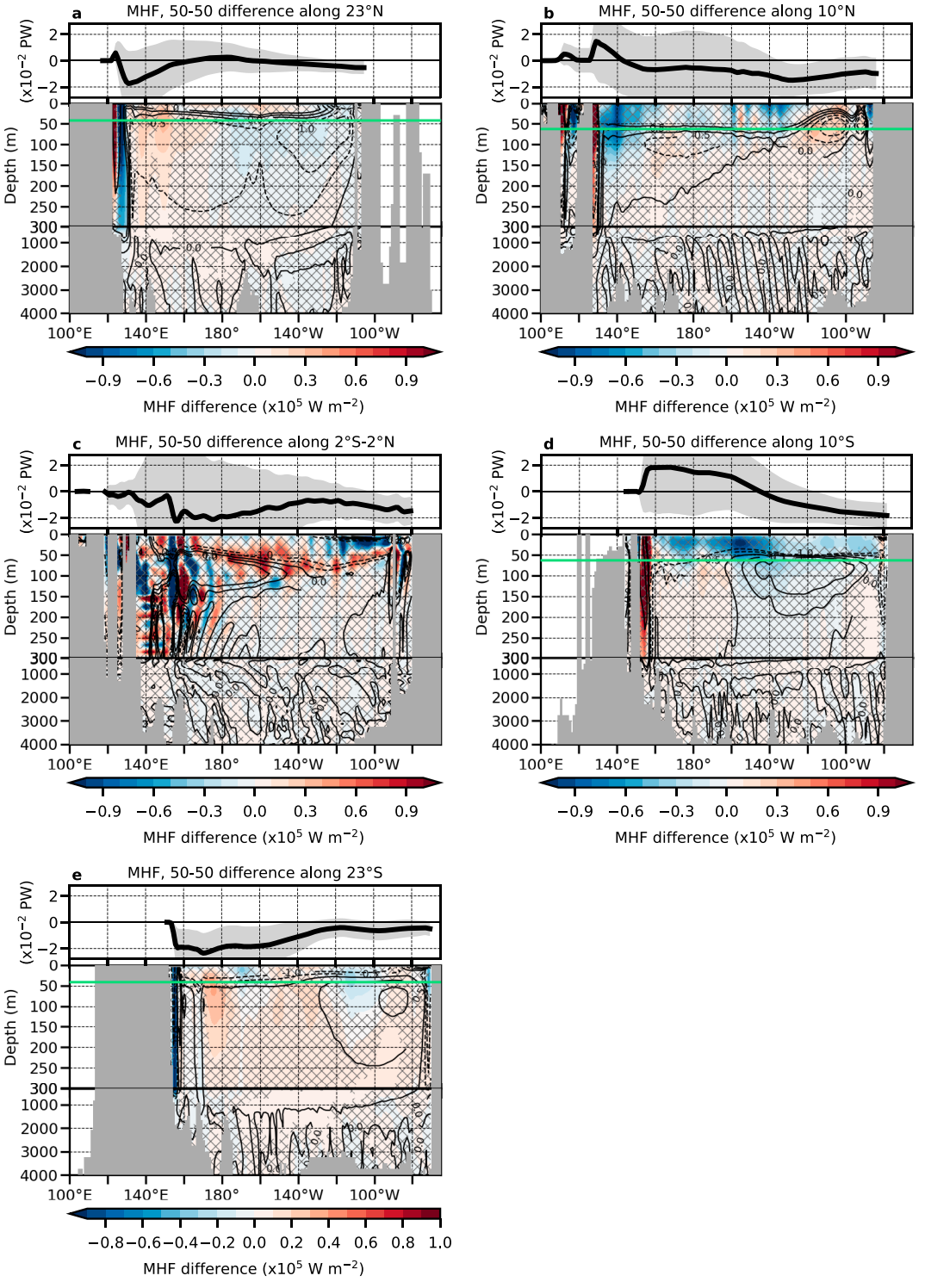

FIG. 10. Difference in CMIP6 and SMBB subensemble means of meridional ocean heat flux (MHF; positive northward; shading) along five latitudes—(a) 23°N, (b) 10°N, (c) equator (2°S–2°N), (d) 10°S, and (e) 23°S—over years 2000–20. In each panel the upper plot shows the eastward cumulative sum of depth-integrated MHF 50–50 difference from the western boundary (i.e., their values at the eastern boundary are identical to Fig. 9d) with shading indicating the estimated two standard deviation ranges ($\pm 2\sigma$) based on the bootstrapping. Climatological-mean (100-ensemble mean) MHFs (10^6 W m^{-2}) are superimposed in the lower plot of each panel as contours [contour levels = (± 100, ± 10, ± 1, ± 0.5, 0)]. Statistically insignificant MHF differences at the 95% confidence level are cross-hatched. The green lines in (a), (b), (d), and (e) indicate approximate Ekman layer depth defined as $\sqrt{2A_V/f}$, where A_V and f are the eddy viscosity ($A_V = 0.05$ m^2 s^{-1}) and the Coriolis parameter, respectively.

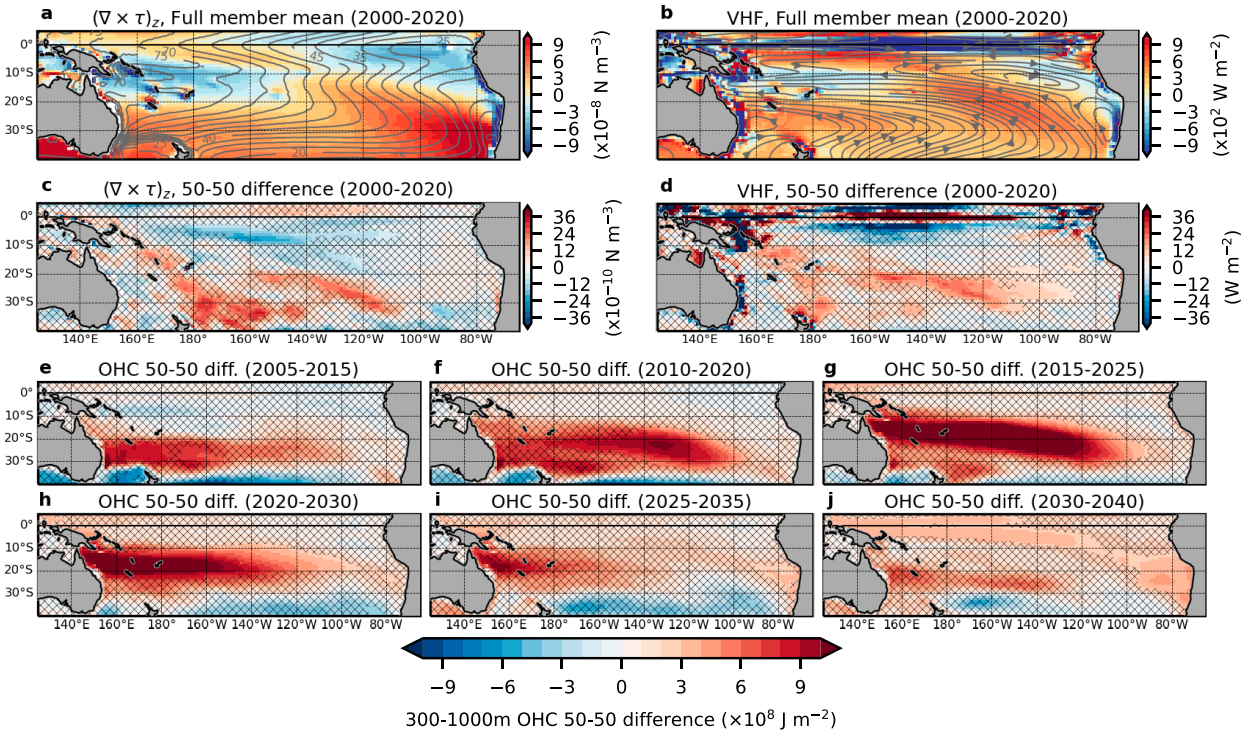

FIG. 11. 100-member ensemble-mean climatology (2000–20) of (a) surface wind stress curl $[(\nabla \times \boldsymbol{\tau})_z]$ and SSH (contours; cm) and (b) 100–300-m-mean vertical heat flux (VHF; positive downward) and streamlines at 300 m depth. Differences in subensemble means (CMIP6 minus SMBB) in (c) $(\nabla \times \boldsymbol{\tau})_z$, (d) VHF, and (e)–(j) subsurface ocean heat content (OHC; 300–1000 m). Statistically insignificant differences at the 95% confidence level are cross-hatched in (c)–(j).

At the equator, the response is more complicated. MHT anomalies associated with the enhanced narrow southward current around 155°E mainly contribute to the net southward CEHT anomaly, with secondary contributions from near-surface southward CEHT anomalies east of 130°W (Fig. 10c). This equatorial behavior, which demonstrates a dominant contribution of the frictional WBC to sustain anomalous CEHT at the equator, is more consistent with and hence supports recent results obtained with a low-resolution idealized atmosphere–ocean coupled model (Green and Marshall 2017; Green et al. 2019), whereas it is not resonant with a framework whereby the CEHT is sustained by a shifting of the STCs themselves (Schneider 2017). That is to say, from the northern boundary of the anomalous CEC (around 30°N) to the southern boundary (near 30°S), the dominant contributions for generating the net southward zonally integrated MHT anomalies differs between the contributions in WBC regions and non-WBC regions, depending on their latitude.

The strong convergence of the southward zonally integrated MHT anomalies south of 10°S (Fig. 9d) implies a downward shunting of heat into the ocean interior, thereby accounting for the accumulation of heat in the low-latitude Pacific (equatorial and South Pacific) already identified in Fig. 6g. For the South Pacific subtropics (from approximately 18° to 40°S), with the exception of the coastal regions, vertical heat flux (VHF) just below the layer where it interacts directly with the atmosphere (below about 100 m depth) corresponds well to what is expected from the surface wind stress curl $[(\nabla \times \boldsymbol{\tau})_z]$ field through Ekman dynamics (Figs. 11a,b). During the period when CMIP6 and SMBB forcings are different, differences between the two 50-member subensembles indicate a positive wind stress curl anomaly over the South Pacific subtropical gyre (Fig. 11c). These positive anomalies enhance the Ekman pumping (downwelling) and hence induce anomalous VHFs that carry more heat into the subsurface layer (Fig. 11d). The heat transported below 300 m depth accumulates within the South Pacific subtropical gyre, and through time is advected along a circulation structure extending to approximately 10°S (Figs. 11e–g). Part of the heat is then transported to the subsurface zone of the equatorial band via the northward NQC/HC and NGCU (Figs. 11h–j). These heat anomalies accumulated within the South Pacific Subtropical Gyre and those that reached below the equatorial thermocline both contribute to the low-latitude Pacific OHC anomalies that persist until the end of the simulation (Fig. 6g and Fig. S6). Over longer time scales than are the main focus of this study, baroclinic wave adjustment associated with an abrupt AMOC change (Timmermann et al. 2005) can also be expected to induce subsurface temperature anomalies in the tropical and South Pacific (Wang et al. 2018). Here, however, we emphasize the importance of the local wind forcing (positive wind stress curl anomalies) in this shorter-time-scale ocean response.

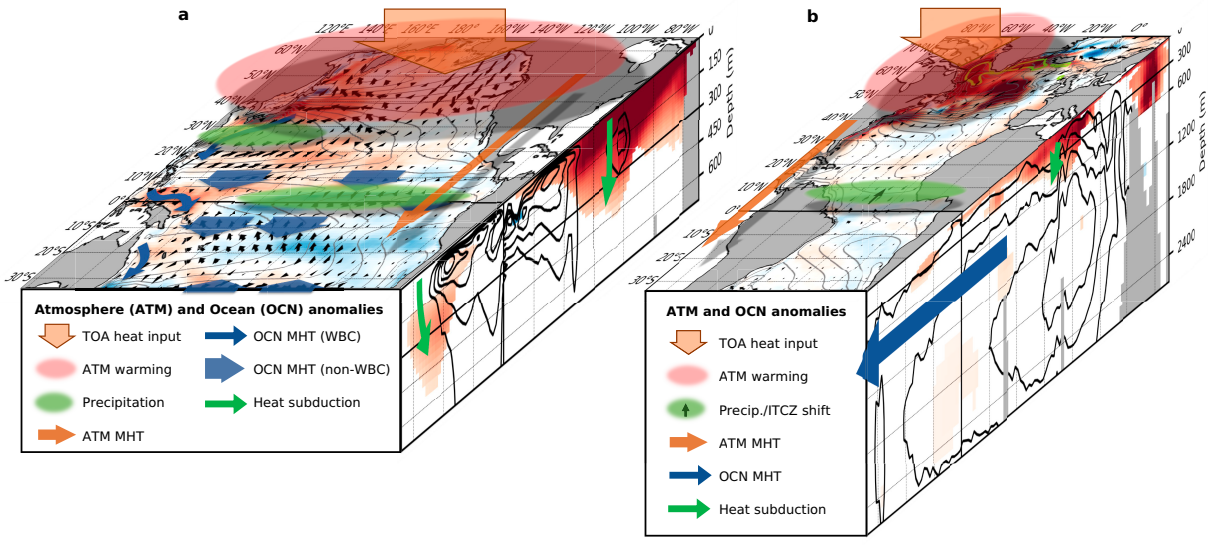

FIG. 12. Schematic figure for illustrating (a) Pacific and (b) Atlantic Ocean responses to the NH decadal warming induced by the high-amplitude BBA emissions variability. The top panels show differences in subensemble-mean (CMIP6 minus SMBB for years 2000–20) net surface heat flux (positive downward) and surface wind as shading and vectors, respectively. The contours in the top panel indicate 100-member mean SSH. In the side panels, differences in subensemble-mean temperature (shading) and MOC (contours) are shown. Note that only negative MOC anomalies from the shading in Fig. 7 are shown as contours.

5. Summary and discussion

We have investigated the ocean response to anomalous NH warming induced by a rectified response to interannual modulations of BBA emissions and corresponding shortwave radiation. We compared two 50-member subensembles of the 100-member CESM2-LE, with their BBA emission forcing differing over 1990–2020. By virtue of having two large sets of simulations with 50 ensemble members each, which were conducted with a fully coupled Earth system model, our experimental design facilitates a clear separation of the forced response to changes in the interannual variability of BBA emissions from background natural variability. The main takeaways of this study are 1) the detailed description of the complexity of the Pacific CEC response and 2) the explanation of the mechanism for heat accumulation at the Pacific subsurface, resulting in the long-lasting oceanic memory of the high-amplitude interannual BBA forcing. Our emphasis on the ocean response to hemispherically asymmetric thermal forcing, especially in the anomalous Pacific CEC, is complementary to previous more atmospherically focused studies that have applied atmosphere–slab ocean coupled models (e.g., Manabe and Broccoli 1985; Chiang et al. 2003; Kang et al. 2008), studies with idealized atmosphere–ocean coupled models (e.g., Green and Marshall 2017), and studies applying state-of-the-art climate models with limited numbers of ensemble members (e.g., White et al. 2018; Yu and Pritchard 2019), as well as studies that have considered longer-time-scale (from interdecadal to equilibrium) responses (e.g., Tomas et al. 2016; Wang et al. 2018, 2022).

Detectable differences in the responses of the Pacific and Atlantic Oceans are summarized schematically in Fig. 12. The initial atmospheric and sea ice responses to anomalous heat input through radiation across the top of the atmosphere in the NH high latitudes are common to both basins (e.g., atmospheric warming, increased in atmospheric southward CEHT, and sea ice melting), but the subsequent ocean responses are notably different between the two basins. In the Atlantic, heat absorbed by the ocean warms the upper part of the North Atlantic and enhances upper ocean stratification (Fig. S7a). Some of the heat is subducted into the subsurface within the subtropical and subpolar gyres (Fig. S7b) and the enhanced stratification slows down the AMOC. The warm anomalies in the upper North Atlantic Ocean are compensated by a reduction in northward ocean heat transport due to the weakened AMOC which occurs broadly across the basin. Subsequent to the time interval when the BBA forcing is different (namely, after the year 2020), part of the forced warm anomaly is sustained in the subsurface for multiple decades (Figs. S7c–f), while the ocean nevertheless continually releases anomalous heat into the atmosphere.

As with the Atlantic, the upper Pacific Ocean is warmed directly during the period when BBA emissions forcing is different (Fig. S6a). In contrast to the Atlantic, however, the anomalous CEC in the Pacific is associated with hemispherically asymmetric trade wind anomalies, characterized by weakened NH trade winds and strengthened SH trade winds. We found that the anomalous CEC and the resultant net southward ocean MHT anomalies covering the tropical Pacific (30°S–30°N) reflect a complex latitude-dependent interplay between the WBCs and the near-surface Ekman transport away from the western boundary regions. The deceleration of the North Pacific subtropical WBC (Kuroshio), a component of the anomalous CEC, reduces northward heat transport into the North Pacific and thereby to an extent partly compensates for the anomalous heat

flux into the North Pacific. Other components of the heat flux perturbation applied across the surface of the North Pacific are subsequently released to the atmosphere and/or transferred into the subsurface (Figs. S6a–c). In the South Pacific, the southward heat transport anomalies converge and by this means heat is shunted into the subsurface. Heat accumulated in the subsurface of the South Pacific subtropical circulation is then partly transported to the layer below the equatorial thermocline via the NGCU, which contributes to the persistent ocean memory (Figs. S6d–f).

The primary factors distinguishing the ocean responses between the Pacific and Atlantic are the presence of a deep MOC structure for the Atlantic relative to the Pacific and the enhanced efficiency in the Pacific of zonally integrated wind stress curl–driven transport anomalies as a consequence of its significantly broader zonal extent. For the present case, the anomalous increase in OHC is smaller in the Atlantic than in the Pacific, even though the Atlantic gains 30% more heat through local surface heat flux anomalies during the period of the high-amplitude BBA emissions variability (Fig. S8). For the Atlantic, the AMOC is able to compensate NH warming anomalies by virtue of not only its access to a deep heat reservoir but also the broad meridional reach of its coherent circulation pattern, meaning that there is more direct leverage for an anomalous OHTC reduction through its southern end (Fig. S8). As the Pacific is a much wider basin than the Atlantic, net CEC anomalies can be more effectively controlled by anomalies in trade wind strength associated with hemispherically asymmetric thermal forcing perturbations.

This study has broader implications for understanding the response of the climate system to BBA emissions. As has been described above, previous studies (Fasullo et al. 2022; DeRepentigny et al. 2022; Kim et al. 2023) have shown that the BBA emissions forcing protocols for CMIP6 (BB4CMIP6) with spurious discontinuities in the variance of BBA emissions are somewhat of a mixed blessing. Despite the increased realism in this forcing during data-rich periods, spurious changes in the amplitude of BBA emissions can lead to detectable mean state changes in a number of important climate variables. Viewing this in a positive light, this sensitivity to large changes in the variance of BBA emissions has also drawn our attention to a previously underappreciated role for BBA emissions in the climate system.

Moving forward, there are two points that we wish to emphasize that are informed by what we have learned thus far. First, the rectified heat anomalies in the atmosphere associated with changes in the interannual variability of BBA emissions are only on the order of 0.4 W m^{-2}, and yet this is sufficient to trigger large-scale adjustment processes reaching into the SH. It is valuable to consider this within the context of volcanic eruptions (Church et al. 2005; Stenchikov et al. 2009) where the short-term intensity of forcing from an individual volcano can be 10 times larger in magnitude (~ -4 W m^{-2} vs $\sim$0.4 W m^{-2} of TOA radiation anomalies), but nevertheless where the net Earth system perturbation can be of similar amplitude [maximum global OHC anomaly of ~ -50 ZJ for a Pinatubo-level volcanic eruption (Stenchikov et al. 2009) compared to $\sim$20 ZJ for increased interannual BBA variability in this study]. Although individual TOA anomalies associated with high-amplitude modulations of BBA emissions variability are smaller, the cumulative impact of intermittent anomalies can have impacts on the system comparable to what is found with large volcanic eruption events.

Second, the fact that the forcing perturbation of CMIP6-SMBB over 1990–2020 spans only 12% of the full 251 years of the CESM2-LE (1850–2100) implies that if realistic BBA emissions were used over the full 1850–2100 period, one might expect that the cumulative ocean heat response to the forcing could be larger than it is under SMBB forcing perturbation considered here. This could be particularly pertinent if interannual variability in BBA emissions were to increase in time with climate change (e.g., van der Werf et al. 2017). With this in mind, it is recommended that the work presented here be extended by considering the climate feedbacks associated with realistic modulations of the frequency and/or intensity of fire occurrence over scenario runs spanning 1850–2100. Such an effort would benefit not only our understanding of the processes that contribute to climate change, but also the development of new protocols that can be applied to the next phase of CMIP.

Acknowledgments. This study was supported by the Institute for Basic Science (IBS), Republic of Korea, under IBS-R028-D1. This material is based upon work supported by the National Center for Atmospheric Research, which is a major facility sponsored by the NSF under Cooperative Agreement 1852977. Malte F. Stuecker was supported by NSF grant AGS-2141728 and NOAA's Climate Program Office's Modeling, Analysis, Predictions, and Projections (MAPP) program grant NA20OAR4310445. This is IPRC publication 1610 and SOEST contribution 11718. Nan A. Rosenbloom and John T. Fasullo are supported by the U.S. Department of Energy, Office of Science, Office of Biological & Environmental Research (BER), Regional and Global Model Analysis (RGMA) component of the Earth and Environmental System Modeling Program under Award Number DE-SC0022070 and National Science Foundation (NSF) IA 1947282. The efforts of John T. Fasullo in this work were supported by NASA Awards 80NSSC21K1191, 80NSSC17K0565, and 80NSSC22K0046. The CESM2 simulations were conducted on the IBS/ICCP supercomputer 'Aleph', 1.43 peta flops high-performance Cray XC50-LC Skylake computing system with 18,720 processor cores, 9.59 PB storage and 43 PB tape archive space. We also acknowledge the support of KREONET.

Data availability statement. The CESM2-LE data are available through NCAR's Climate Data Gateway at https://www.earthsystemgrid.org/dataset/ucar.cgd.cesm2le.output.html.

REFERENCES

Archibald, S., C. E. R. Lehmann, J. L. Gómez-Dans, and R. A. Bradstock, 2013: Defining pyromes and global syndromes of fire regimes. *Proc. Natl. Acad. Sci. USA*, **110**, 6442–6447, https://doi.org/10.1073/pnas.1211466110.

Biastoch, A., C. W. Böning, J. Getzlaff, J.-M. Molines, and G. Madec, 2008: Causes of interannual–decadal variability in the meridional overturning circulation of the midlatitude North Atlantic Ocean. *J. Climate*, **21**, 6599–6615, https://doi.org/10.1175/2008JCLI2404.1.

Bogenschutz, P. A., A. Gettelman, C. Hannay, V. E. Larson, R. B. Neale, C. Craig, and C.-C. Chen, 2018: The path to CAM6: Coupled simulations with CAM5.4 and CAM5.5. *Geosci. Model Dev.*, **11**, 235–255, https://doi.org/10.5194/gmd-11-235-2018.

Broccoli, A. J., K. A. Dahl, and R. J. Stouffer, 2006: Response of the ITCZ to Northern Hemisphere cooling. *Geophys. Res. Lett.*, **33**, L01702, https://doi.org/10.1029/2005GL024546.

Chiang, J. C. H., and A. R. Friedman, 2012: Extratropical cooling, interhemispheric thermal gradients, and tropical climate change. *Annu. Rev. Earth Planet. Sci.*, **40**, 383–412, https://doi.org/10.1146/annurev-earth-042711-105545.

——, M. Biasutti, and D. S. Battisti, 2003: Sensitivity of the Atlantic intertropical convergence zone to last glacial maximum boundary conditions. *Paleoceanogr. Paleoclimatol.*, **18**, 1094, https://doi.org/10.1029/2003PA000916.

Church, J. A., N. J. White, and J. M. Arblaster, 2005: Significant decadal-scale impact of volcanic eruptions on sea level and ocean heat content. *Nature*, **438**, 74–77, https://doi.org/10.1038/nature04237.

Cravatte, S., A. Ganachaud, Q.-P. Duong, W. S. Kessler, G. Eldin, and P. Dutrieux, 2011: Observed circulation in the Solomon Sea from SADCP data. *Prog. Oceanogr.*, **88**, 116–130, https://doi.org/10.1016/j.pocean.2010.12.015.

Danabasoglu, G., S. C. Bates, B. P. Briegleb, S. R. Jayne, M. Jochum, W. G. Large, S. Peacock, and S. G. Yeager, 2012: The CCSM4 ocean component. *J. Climate*, **25**, 1361–1389, https://doi.org/10.1175/JCLI-D-11-00091.1.

——, and Coauthors, 2020: The Community Earth System Model version 2 (CESM2). *J. Adv. Model. Earth Syst.*, **12**, e2019MS001916, https://doi.org/10.1029/2019MS001916.

DeRepentigny, P., and Coauthors, 2022: Enhanced simulated early 21st century Arctic sea ice loss due to CMIP6 biomass burning emissions. *Sci. Adv.*, **8**, eabo2405, https://doi.org/10.1126/sciadv.abo2405.

Deser, C., R. A. Tomas, and L. Sun, 2015: The role of ocean–atmosphere coupling in the zonal-mean atmospheric response to Arctic sea ice loss. *J. Climate*, **28**, 2168–2186, https://doi.org/10.1175/JCLI-D-14-00325.1.

Eyring, V., S. Bony, G. A. Meehl, C. A. Senior, B. Stevens, R. J. Stouffer, and K. E. Taylor, 2016: Overview of the Coupled Model Intercomparison Project Phase 6 (CMIP6) experimental design and organization. *Geosci. Model Dev.*, **9**, 1937–1958, https://doi.org/10.5194/gmd-9-1937-2016.

Fasullo, J. T., J.-F. Lamarque, C. Hannay, N. Rosenbloom, S. Tilmes, P. DeRepentigny, A. Jahn, and C. Deser, 2022: Spurious late historical-era warming in CESM2 driven by prescribed biomass burning emissions. *Geophys. Res. Lett.*, **49**, e2021GL097420, https://doi.org/10.1029/2021GL097420.

Green, B., and J. Marshall, 2017: Coupling of trade winds with ocean circulation damps ITCZ shifts. *J. Climate*, **30**, 4395–4411, https://doi.org/10.1175/JCLI-D-16-0818.1.

——, ——, and J.-M. Campin, 2019: The 'sticky' ITCZ: Ocean-moderated ITCZ shifts. *Climate Dyn.*, **53** (1–2), 1–19, https://doi.org/10.1007/s00382-019-04623-5.

Hawcroft, M., J. M. Haywood, M. Collins, and A. Jones, 2018: The contrasting climate response to tropical and extratropical energy perturbations. *Climate Dyn.*, **51**, 3231–3249, https://doi.org/10.1007/s00382-018-4076-8.

Heyblom, K. B., H. A. Singh, P. J. Rasch, and P. DeRepentigny, 2022: Increased variability of biomass burning emissions in CMIP6 amplifies hydrologic cycle in the CESM2 large ensemble. *Geophys. Res. Lett.*, **49**, e2021GL096868, https://doi.org/10.1029/2021GL096868.

Hunke, E. C., W. H. Lipscomb, A. K. Turner, N. Jeffery, and S. Elliott, 2015: CICE: The Los Alamos Sea Ice Model documentation and software user's manual, version 5.1. Doc. LA-CC-06-012, 116 pp., https://www.osti.gov/biblio/1364126.

Kang, S. M., 2020: Extratropical influence on the tropical rainfall distribution. *Curr. Climate Change Rep.*, **6**, 24–36, https://doi.org/10.1007/s40641-020-00154-y.

——, I. M. Held, D. M. W. Frierson, and M. Zhao, 2008: The response of the ITCZ to extratropical thermal forcing: Idealized slab-ocean experiments with a GCM. *J. Climate*, **21**, 3521–3532, https://doi.org/10.1175/2007JCLI2146.1.

——, Y. Shin, and S.-P. Xie, 2018: Extratropical forcing and tropical rainfall distribution: Energetics framework and ocean Ekman advection. *npj Climate Atmos. Sci.*, **1**, 20172, https://doi.org/10.1038/s41612-017-0004-6.

——, S.-P. Xie, C. Deser, and B. Xiang, 2021: Zonal mean and shift modes of historical climate response to evolving aerosol distribution. *Sci. Bull.*, **66**, 2405–2411, https://doi.org/10.1016/j.scib.2021.07.013.

Kim, J.-E., and Coauthors, 2023: Interannual fires as a source for subarctic summer decadal climate variability mediated by permafrost thawing. *npj Climate Atmos. Sci.*, **6**, 84, https://doi.org/10.1038/s41612-023-00415-1.

Lamarque, J.-F., and Coauthors, 2010: Historical (1850–2000) gridded anthropogenic and biomass burning emissions of reactive gases and aerosols: Methodology and application. *Atmos. Chem. Phys.*, **10**, 7017–7039, https://doi.org/10.5194/acp-10-7017-2010.

Lawrence, D. M., and Coauthors, 2019: The Community Land Model version 5: Description of new features, benchmarking, and impact of forcing uncertainty. *J. Adv. Model. Earth Syst.*, **11**, 4245–4287, https://doi.org/10.1029/2018MS001583.

Manabe, S., and A. J. Broccoli, 1985: The influence of continental ice sheets on the climate of an ice age. *J. Geophys. Res.*, **90**, 2167–2190, https://doi.org/10.1029/JD090iD01p02167.

McCreary, J. P., Jr., and P. Lu, 1994: Interaction between the subtropical and equatorial ocean circulations: The subtropical cell. *J. Phys. Oceanogr.*, **24**, 466–497, https://doi.org/10.1175/1520-0485(1994)024<0466:IBTSAE>2.0.CO;2.

Miyama, T., J. P. McCreary Jr., T. G. Jensen, J. Loschnigg, S. Godfrey, and A. Ishida, 2003: Structure and dynamics of the Indian-Ocean cross-equatorial cell. *Deep-Sea Res. II*, **50**, 2023–2047, https://doi.org/10.1016/S0967-0645(03)00044-4.

Pillar, H. R., P. Heimbach, H. L. Johnson, and D. P. Marshall, 2016: Dynamical attribution of recent variability in Atlantic overturning. *J. Climate*, **29**, 3339–3352, https://doi.org/10.1175/JCLI-D-15-0727.1.

Rabin, S. S., and Coauthors, 2017: The Fire Modeling Intercomparison Project (FireMIP), phase 1: Experimental and analytical protocols with detailed model descriptions. *Geosci. Model Dev.*, **10**, 1175–1197, https://doi.org/10.5194/gmd-10-1175-2017.

Rodgers, K. B., and Coauthors, 2021: Ubiquity of human-induced changes in climate variability. *Earth Syst. Dyn.*, **12**, 1393–1411, https://doi.org/10.5194/esd-12-1393-2021.

Sato, O. T., P. S. Polito, and W. Timothy Liu, 2002: Intradecadal variability in the Ekman heat flux from scatterometer winds. *Geophys. Res. Lett.*, **29**, 1831, https://doi.org/10.1029/2002GL014775.

Schneider, T., 2017: Feedback of atmosphere-ocean coupling on shifts of the intertropical convergence zone. *Geophys. Res. Lett.*, **44**, 11 644–11 653, https://doi.org/10.1002/2017GL075817.

——, T. Bischoff, and G. H. Haug, 2014: Migrations and dynamics of the intertropical convergence zone. *Nature*, **513**, 45–53, https://doi.org/10.1038/nature13636.

Smith, R., and Coauthors, 2010: The Parallel Ocean Program (POP) reference manual: Ocean component of the Community Climate System Model (CCSM). LAUR-10-01853, 141 pp., http://n2t.net/ark:/85065/d70g3j4h.

Stenchikov, G., T. L. Delworth, V. Ramaswamy, R. J. Stouffer, A. Wittenberg, and F. Zeng, 2009: Volcanic signals in oceans. *J. Geophys. Res.*, **114**, D16104, https://doi.org/10.1029/2008JD011673.

Timmermann, A., M. Latif, R. Voss, and A. Grötzner, 1998: Northern Hemispheric interdecadal variability: A coupled air–sea mode. *J. Climate*, **11**, 1906–1931, https://doi.org/10.1175/1520-0442(1998)011%3C1906:NHIVAC%3E2.0.CO;2.

——, S.-I. An, U. Krebs, and H. Goosse, 2005: ENSO suppression due to weakening of the North Atlantic thermohaline circulation. *J. Climate*, **18**, 3122–3139, https://doi.org/10.1175/JCLI3495.1.

Tomas, R. A., C. Deser, and L. Sun, 2016: The role of ocean heat transport in the global climate response to projected Arctic Sea ice loss. *J. Climate*, **29**, 6841–6859, https://doi.org/10.1175/JCLI-D-15-0651.1.

van der Werf, G. R., and Coauthors, 2017: Global fire emissions estimates during 1997–2016. *Earth Syst. Sci. Data*, **9**, 697–720, https://doi.org/10.5194/essd-9-697-2017.

van Marle, M. J. E., and Coauthors, 2017: Historic global biomass burning emissions for CMIP6 (BB4CMIP) based on merging satellite observations with proxies and fire models (1750–2015). *Geosci. Model Dev.*, **10**, 3329–3357, https://doi.org/10.5194/gmd-10-3329-2017.

Wang, K., C. Deser, L. Sun, and R. A. Tomas, 2018: Fast response of the tropics to an abrupt loss of Arctic sea ice via ocean dynamics. *Geophys. Res. Lett.*, **45**, 4264–4272, https://doi.org/10.1029/2018GL077325.

——, L. Wu, H. Liu, B. Dan, H. Dai, and C. Deser, 2022: Contrary responses of the Gulf Stream and the Kuroshio to Arctic sea ice loss. *Atmosphere*, **13**, 514, https://doi.org/10.3390/atmos13040514.

White, R. H., A. A. McFarlane, D. M. W. Frierson, S. M. Kang, Y. Shin, and M. Friedman, 2018: Tropical precipitation and cross-equatorial heat transport in response to localized heating: Basin and hemisphere dependence. *Geophys. Res. Lett.*, **45**, 11 949–11 958, https://doi.org/10.1029/2018GL078781.

Yeager, S., and G. Danabasoglu, 2014: The origins of late-twentieth-century variations in the large-scale North Atlantic circulation. *J. Climate*, **27**, 3222–3247, https://doi.org/10.1175/JCLI-D-13-00125.1.

Yoshimori, M., A. Abe-Ouchi, H. Tatebe, T. Nozawa, and A. Oka, 2018: The importance of ocean dynamical feedback for understanding the impact of mid–high-latitude warming on tropical precipitation change. *J. Climate*, **31**, 2417–2434, https://doi.org/10.1175/JCLI-D-17-0402.1.

Yu, S., and M. S. Pritchard, 2019: A strong role for the AMOC in partitioning global energy transport and shifting ITCZ position in response to latitudinally discrete solar forcing in CESM1.2. *J. Climate*, **32**, 2207–2226, https://doi.org/10.1175/JCLI-D-18-0360.1.